

# 000 001 002 003 004 005 006 007 008 009 010 011 012 013 014 015 016 017 018 019 020 021 022 023 024 025 026 027 028 029 030 031 032 033 034 035 036 037 038 039 040 041 042 043 044 045 046 047 048 049 050 051 052 053 OTTERS: AN ENERGY-EFFICIENT SPIKING TRANSFORMER VIA OPTICAL TIME-TO-FIRST-SPIKE ENCODING

Anonymous authors

Paper under double-blind review

## ABSTRACT

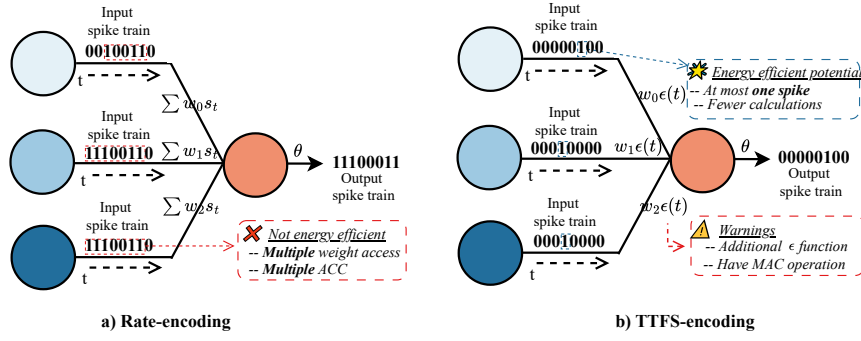
Spiking neural networks (SNNs) promise high energy efficiency, particularly with time-to-first-spike (TTFS) encoding, which maximizes sparsity by emitting at most one spike per neuron. However, such energy advantage is often unrealized because inference requires evaluating a temporal decay function and subsequent multiplication with the synaptic weights. This paper challenges this costly approach by repurposing a physical hardware ‘bug’, namely, the natural signal decay in optoelectronic devices, as the core computation of TTFS. We fabricated a custom indium oxide optoelectronic synapse, showing how its natural physical decay directly implements the required temporal function. By treating the device’s analog output as the fused product of the synaptic weight and temporal decay, optoelectronic synaptic TTFS (named Otters) eliminates these expensive digital operations. To use the Otters paradigm in complex architectures like the transformer, which are challenging to train directly due to the sparsity issue, we introduce a novel quantized neural network-to-SNN conversion algorithm. This complete hardware-software co-design enables our model to achieve state-of-the-art accuracy across seven GLUE benchmark datasets and demonstrates a  $1.77\times$  improvement in energy efficiency over previous leading SNNs, based on a comprehensive analysis of compute, data movement, and memory access costs using energy measurements from a commercial 22nm process. Our work thus establishes a new paradigm for energy-efficient SNNs, translating fundamental device physics directly into powerful computational primitives. All codes and data are open source<sup>1</sup>.

## 1 INTRODUCTION

Large language models (LLMs) have demonstrated remarkable capabilities, yet their immense computational and energy costs hinder their deployment in resource-constrained environments such as edge devices (Lin et al., 2023; Jegham et al., 2025). This critical challenge has spurred research on more efficient, brain-inspired architectures, with spiking neural networks (SNNs) emerging as a promising candidate (Xing et al., 2024a; Tang et al., 2025; Xing et al., 2024b). SNNs are known for their potential energy efficiency, which stems from sparse, event-driven computations that use addition instead of expensive multiplications. However, realizing this efficiency in practice is complex and depends heavily on the encoding scheme used (Yan et al., 2024). In conventional rate-coded SNNs, information is encoded in the number of spikes in a fixed time window. This approach necessitates multiple memory accesses for weights and frequent data movement on each spikes, which may negate the benefits of the sparse computation. Temporal coding schemes, specifically, time-to-first-spike (TTFS), offer a potentially more efficient alternative. By encoding information in the precise timing of a single spike, a TTFS-SNN neuron fires at most once per activation cycle. This maximizes sparsity, dramatically reducing spike count and the associated data movement costs, making TTFS a theoretically optimal encoding for energy efficiency (Yu et al., 2023; Zhao et al., 2025).

<sup>1</sup><https://anonymous.4open.science/r/ICLR26Otters-26F1/README.md>

054  
055  
056  
057  
058  
059  
060  
061  
062  
063  
064

065  
066  
067  
Figure 1: Rate encoding vs TTFS encoding  
068  
069

070 However, there are hidden costs behind this theoretical efficiency. In TTFS, information is encoded  
071 by mapping a spike’s timing to its importance; typically, the earlier a spike arrives, the larger the  
072 numerical value it represents. To implement this principle, the network usually need to perform an  
073 extra computational step to convert the raw arrival time of each spike into a corresponding value.  
074 This is done using a decay function (e.g.,  $\epsilon(t) = e^{-t}$  or  $T - t$ ) whose output is then multiplied by  
075 the synaptic weight ( $w \cdot \epsilon(t)$ ) (Wei et al., 2023; Che et al., 2024b). This conversion process requires  
076 energy to calculate the decay function itself, and it re-introduces the multiplication operations that  
077 SNNs are designed to avoid. This practical drawback negates the energy savings from sparsity and  
078 thus raising a critical question: how can we benefit from the sparsity of TTFS but avoid the costly  
079 computation? Recognizing that the costly term  $w \cdot \epsilon(t)$  is a value that predictably decreases over time,  
080 our answer lies not in optimizing the digital computation but finding a physical analog to simulate  
081 this process. This approach leads us to optoelectronic synapses, which are attractive for their fJ-level  
082 energy consumption and high resistance to electromagnetic interference (Li et al., 2024b). Notably,  
083 while this field has traditionally focused on suppressing their natural signal decay (volatility) to  
084 create stable memories (Alqahtani et al., 2025), we embrace this decay. We recognize it not as a  
085 bug, but as the exactly physical implementation of the temporal decay function that TTFS requires.  
086 To implement this principle, we fabricated a custom  $In_2O_3$  optoelectronic synapse. Our method,  
087 Otters, uses the natural decay of this device’s optical signal to perform the required computation.  
088 This approach fundamentally integrates storage and computation into a single physical step, solving  
089 the overhead problem of traditional TTFS.

090 While our Otters hardware solves the computational overhead of TTFS, a second major barrier re-  
091 mains: the inherent difficulty of training such networks, especially for complex architectures like  
092 the Transformer. Directly training SNNs is challenging. In event-driven learning, error backprop-  
093 agation depends on spike timing; if a neuron fires too sparsely or not at all, it fails to learn. This  
094 “over-sparsity” problem can severely limit the model’s performance and even lead to training fail-  
095 ure (Wei et al., 2023). To sidestep this issue, we employ a quantized neural network(QNN)-to-SNN  
096 conversion methodology. We first train a QNN and then convert its weights to our Otters SNN,  
097 avoiding the pitfalls of direct training in the spiking domain. To further maximize efficiency, we use  
098 knowledge distillation to train a highly compressed model with 1-bit weights and 1-bit key/value  
099 (KV) projections. Our complete hardware-software co-design, combining the Otters synapse with  
100 our QNN-to-SNN conversion pipeline, establishes a new state of the art for spiking language models.  
101 Evaluated on the GLUE benchmark, Otters achieves average accuracy of 3% higher than previous  
102 leading SNNs while demonstrating a 1.77-3.04× improvement in energy efficiency compared to  
103 baselines like Sorbet and SpikingLM (Tang et al., 2025; Xing et al., 2024b). Notably, this energy  
104 efficiency gain is validated by a rigorous and comprehensive analysis that moves beyond the sim-  
105 plistic metrics common in prior SNN research. While previous work often only counted compute  
106 operations (e.g., additions vs. multiplications), our analysis provides a more realistic estimate. It  
107 is grounded in measurements from a commercial 22nm process and provides a full accounting of  
108 compute, data movement, and memory access costs, making our efficiency claims robust.

We also investigate the Otters paradigm’s sensitivity to the hardware noise inherent in analog de-  
vices. Our initial analysis shows that, on the SST-2 benchmark, the baseline model’s performance

108 begins to degrade with around 5% variation in key physical parameters. To improve the robustness,  
 109 we propose Hardware-Aware Training, a method where we introduce different levels of simulated  
 110 Gaussian noise during the training process. This approach enhances the model’s resilience, enabling  
 111 it to maintain robust performance in noisy conditions, demonstrating a practical path toward robust  
 112 real-world deployment.

## 114 2 PRELIMINARY

### 116 2.1 OPTOELECTRONIC SYNAPSE

118 An optoelectronic synapse is a neuromorphic device that emulates biological synaptic functions by  
 119 using optical signals to modulate its electrical conductance. These devices are renowned for their  
 120 potential for extreme energy efficiency, broader bandwidth and faster signal transmission in neu-  
 121 romorphic computing, which are key advantages over purely electronic counterparts (Xie et al.,  
 122 2024; Wang et al., 2023). Recent studies have reported energy consumption reaching the femtojoule  
 123 (fJ)/spike level, comparable to biological synapses and substantially lower than conventional CMOS  
 124 neuron devices (Shi et al., 2022; Wang et al., 2024). Among various implementations, oxide thin-  
 125 film transistors (TFT) are regarded as viable candidates for optoelectronic synapses due to their low  
 126 leakage current and capability for large-area, flexible fabrication. Solution-based fabrication further  
 127 offers the advantages of low cost, simplified processing, and facile compositional control. Previous  
 128 reports have shown that solution-processed devices exhibit uniform performance, operational stabil-  
 129 ity, and low energy consumption (Li et al., 2025). Building upon these advances, this work employs  
 130 the mature and reliable oxide-TFT platform to develop the Otters spiking neuron.

### 131 2.2 TIME TO FIRST SPIKE SNN

133 In contrast to rate-based encoding, which uses the frequency of spikes to represent information,  
 134 TTFS encoding leverages the precise timing of a single spike. The core principle is that a stronger  
 135 input stimulus causes a neuron’s membrane potential to rise faster, reaching its firing threshold  
 136 sooner. Thus, the information is encoded in the arrival time of the first—and only—spike within a  
 137 given time window,  $T$ . This approach maximizes temporal sparsity and is highly efficient, as each  
 138 neuron fires at most once (Che et al., 2024a).

139 The operation of a standard TTFS neuron involves two phases. First, the neuron integrates incom-  
 140 ing spikes, updating its membrane potential  $V_j^l(t)$ . Second, it compares this potential to a firing  
 141 threshold  $\theta^l(t)$ . A spike is generated at the first time step  $t$  where the potential meets or exceeds the  
 142 threshold:

$$143 \quad s_j^l(t) = \begin{cases} 1, & \text{if } V_j^l(t) \geq \theta^l(t) \\ 0, & \text{otherwise} \end{cases} \quad (1)$$

146 However, the asynchronous nature of SNNs, combined with the “fire-as-early-as-possible” objective  
 147 of TTFS, can lead to another problem. If a presynaptic neuron fires after a postsynaptic neuron  
 148 has already fired, its spike becomes invalid for membrane potential accumulation. To solve this,  
 149 we employ a Dynamic Firing Threshold (DFT) model that enforces a synchronous, layer-by-layer  
 150 processing schedule (Wei et al., 2023). The threshold for any neuron in layer  $l$  is set to infinity  
 151 outside of a designated time window, effectively ensuring that layer  $l$  is only active from time  $T \cdot l$   
 152 to  $T \cdot (l + 1)$ :

$$153 \quad \theta^l(t) = \begin{cases} \theta_{\text{dynamic}}^l(t), & \text{if } T \cdot l \leq t \leq T \cdot (l + 1) \\ +\infty, & \text{otherwise} \end{cases} \quad (2)$$

155 This scheduling guarantees that all spikes from a preceding layer are processed before the current  
 156 layer can fire, thus preserving the valid causal relationship.

## 158 3 METHODS

161 This section details the methodology behind Otters. We first describe the core of our model: the  
 162 optoelectronic synapse and the neuron model that performs the TTFS computation (Section 3.1). We

then explain how these components are assembled into the complete optimized spiking Transformer architecture (Section 3.2), and then, we outline the QNN-to-SNN conversion pipeline used to build the Otters model (Section 3.3). Finally, we present the framework for the comprehensive energy analysis used to validate our model’s efficiency (Section 3.4).

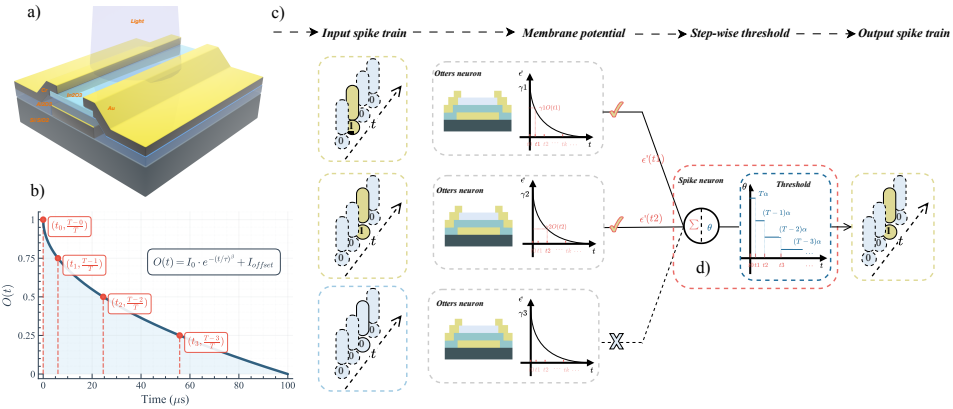


Figure 2: Device and workflow: (a) the custom-fabricated  $\text{In}_2\text{O}_3$  thin-film transistor (TFT); (b) measured decay curve of the device response; (c) Otters neuron workflow.

### 3.1 OTTERS SPIKING NEURON

The core of our method is the Otters optoelectronic synapse, a hardware element that physically implements the time-modulated synaptic dynamics required for TTFS computation. Each synapse is composed of two main parts: a custom-fabricated Indium Oxide Thin-Film Transistor that provides a physical signal decay, and an analog-to-digital converter (ADC) that map and scale the analog signal to digital. Fabrication details for the device in Fig. 2(a) are provided in Appendix A.1. To ensure a deterministic response, the TFT is operated with a fixed light intensity, yielding a consistent non-linear decay curve, modeled by the function  $O(t) = I_0 \cdot e^{-(t/\tau)^\beta} + I_{\text{offset}}$  (Li et al., 2024a; Liang et al., 2022). We fit the model parameters by minimizing the sum of squared residuals using the differential evolution algorithm, yielding:  $I_0 = 110.989$ ,  $\tau = 1.3425$ ,  $\beta = 0.495$ , and  $I_{\text{offset}} = -109.989$ , showing in Figure 2(b). Thus, the TFT’s current decay over time naturally forms the temporal component of the post-synaptic potential (PSP).

However, the physical non-linearity of the device presents a critical design challenge. For our QNN-to-SNN conversion to be lossless, the information encoded by a spike’s timing must map to a set of uniformly spaced logical values. Specifically, a spike occurring at a physical time  $t_k$  must represent the quantized value  $(T - k)/T$ . The device’s non-linear decay,  $O(t)$ , means that the physical times  $t_k$  at which the device output naturally equals these target values are themselves non-uniformly spaced. A naive approach using a constant threshold and uniform time sampling would therefore fail to establish the required functional equivalence.

Therefore, our solution is to reconcile the non-linear device physics with the linear encoding requirement. Instead of implementing a complex, non-uniform clock, we engineer a dynamic, step-wise decreasing firing threshold,  $\theta^l(t)$ , while operating the system on a standard, uniform physical clock. This threshold is designed to change its value only at the pre-calculated time points  $\{t_k\}$  which are derived from the inverse of the physical decay function. This design ensures that the firing condition where the membrane potential exceeding the threshold can only be met at one of these discrete moments  $t_k$ . The neuron fires at the first such time point where its accumulated potential is sufficient. Consequently, the output spike time  $t_k$  can encode the intended quantized value  $(T - k)/T$ . Because this encoding scheme is applied consistently throughout the network, the output spike of one layer provides a correctly timed and valued input to the next, ensuring the integrity of information propagation across the entire architecture. The full mathematical formulation of this threshold will be defined in our conversion methodology in Section 3.3.

The ADC implements a  $\gamma_{ij}^l$  times scaling mapping from the physical decay to a digital post-synaptic potential (PSP). Thus, the full PSP  $\epsilon'$  generated by a presynaptic spike is therefore the direct analog output of the synapse at the time of arrival:

$$\epsilon'(t) = \gamma_{ij}^l \cdot O(t) \quad (3)$$

The membrane potential  $V_j^l(t)$  of neuron  $j$  accumulates these PSPs. At each discrete physical time step  $t$ , the potential is updated based on incoming spikes:

$$V_j^l(t) = V_j^l(t-1) + \sum_{i \text{ s.t. } s_i^{l-1}(t)=1} \epsilon'(t) \quad (4)$$

A neuron fires when its membrane potential first meets or exceeds the dynamic threshold. This spike time,  $t_{\text{spike},j}^l$ , corresponds to the first logical timestep  $k$  where the condition is met:

$$t_{\text{spike},j}^l = \min\{t_k | V_j^l \geq \theta^l(t_k)\} \quad (5)$$

In adherence with the TTFS paradigm, the neuron is deactivated after firing to ensure at most one spike per inference cycle. Algorithm 1 in appendix formally describes this forward pass.

### 3.2 NETWORK STRUCTURE

A primary challenge in creating a spiking Transformer is the matrix multiplication required for self-attention score calculation ( $Q \cdot K^T$ ). While some rate-coded SNNs can simplify this by treating one matrix as a binary spike train (turning multiplication into selective addition), this approach is incompatible with TTFS encoding, which requires decoding spikes into non-binary values. To overcome the problem, we quantize the key ( $K$ ) and value ( $V$ ) projections to a single bit,  $\{+1, -1\}$ . Consequently, the dot product with a TTFS-encoded query ( $Q$ ) is computed using only selective, additions and subtractions. This allows us to eliminate the multiplication bottleneck while still benefiting from the high sparsity of TTFS. To implement this 1-bit attention mechanism efficiently, we designed a supporting dataflow architecture inspired by the Canon architecture (Bai et al., 2025), as illustrated in Figure 3. During inference, the binary  $K$  (or  $V$ ) vectors are pre-loaded into the local memory of a Processing Element (PE) array. The TTFS-encoded input stream (representing  $Q$ ) is broadcast to the PEs. As shown, each PE computes a partial sum by accumulating its local  $K$  values only at the time steps corresponding to incoming spikes. These partial sums are then passed between PEs for final accumulation. This architecture minimizes data movement and leverages the spatio-temporal sparsity of the TTFS input for energy efficiency.

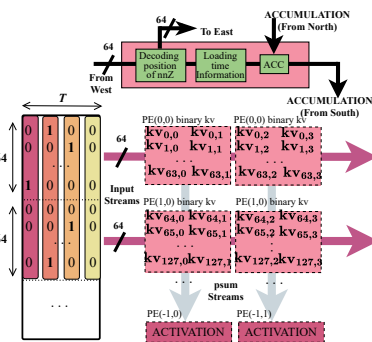


Figure 3: Scores calculations

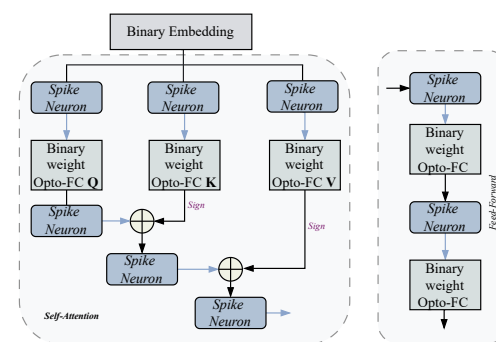


Figure 4: Otters-based transformer structure

This self-attention module, along with feed-forward layers built from our Opto-FC and spiking neuron primitives, forms the complete Otters Transformer architecture shown in Figure 4.

### 3.3 QNN-TO-SNN CONVERSION

To overcome the challenges of direct SNN training, we employ a QNN-to-SNN conversion methodology. We first train a QNN and then map its learned parameters to an equivalent Otters SNN,

ensuring the two networks are functionally identical. To formalize this relationship, we first define the specific QNN layer architecture that enables this equivalence. A compatible QNN layer computes its output  $x_{q,j}^l$  for neuron  $j$  as follows:

$$a_j^l = \sum_i w_{ij}^l x_{q,i}^{l-1} + b_j^l \quad (6)$$

$$x_{q,j}^l = Q(a_j^l) = \alpha^l \cdot \text{Clip}(\lfloor \frac{a_j^l}{\alpha^l} \rfloor, 0, 2^n - 1) \quad (7)$$

where  $a_j^l$  is the pre-activation,  $w_{ij}^l$  are the weights,  $b_j^l$  is the bias, and  $\alpha^l$  is the quantization scaling factor for layer  $l$ . With this structure established, we can now state the proposition that governs the exact conversion from the trained QNN to the Otters SNN:

**Proposition 1.** *An Otters SNN layer (as defined in Section 3.1) is functionally equivalent to a trained  $n$ -bit QNN layer (as defined above) if its parameters are constructed as follows:*

1. *The number of discrete time steps in the SNN simulation window,  $T$ , is set to match the number of positive quantization levels of the  $n$ -bit QNN:  $T = 2^n - 1$ .*
2. *The mapping from a logical time step  $k \in \{0, 1, \dots, T - 1\}$  to a physical spike time  $t_k$  is defined such that the device's output at that instant,  $O(t_k)$ , is linearly proportional to the remaining time in the window:  $O(t_k) = \frac{T-k}{T}$ .*
3. *The SNN's physical scaling factor for the synapse connecting neuron  $i$  in layer  $l - 1$  to neuron  $j$  in layer  $l$ ,  $\gamma_{ij}^l$ , is set based on the corresponding QNN weight and the quantization scale of the previous layer:  $\gamma_{ij}^l = w_{ij}^l \cdot \alpha^{l-1} \cdot T$ .*
4. *The SNN's firing threshold for neuron  $j$  in layer  $l$  is a step-wise decreasing function of time, defined as:  $\theta^l(t) = \alpha^l \cdot (T - k)$ , for  $t_k \leq t < t_{k+1}$ .*

The proof proceeds in two steps. First, during integration, we show that the accumulated membrane potential  $V_j^l$  in an SNN neuron is numerically identical to the corresponding QNN neuron's pre-activation value  $a_j^l$ . We binarize weights  $w_{ij}^l$  to reduce energy and increase the reuse of factor  $\gamma_{ij}^l$ . Second, during firing, we show that the engineered, time-dependent threshold  $\theta_j^l(t)$  compensates for the device's intrinsic non-linearity by permitting firing only at pre-calculated time points,  $t_k$ , derived from the inverse of the physical decay function. This mechanism ensures the SNN neuron fires at a time  $t_{\text{spike},j}^l$  that precisely encodes the QNN's quantized output  $x_{q,j}^l$ . A detailed proof is provided in the Appendix A.2.

### 3.4 ENERGY ANALYSIS

To evaluate the efficiency of our approach, we formulate an analytical energy model. The total inference energy ( $E$ ) is decomposed into three primary components: computation energy ( $E_{\text{Compute}}$ ), data movement energy ( $E_{\text{Data}}$ ), and analog energy ( $E_{\text{Analog}}$ ) (Yan et al., 2024; Dampfhofer et al., 2022). The computation energy,  $E_{\text{Compute}}$ , accounts for arithmetic operations of additions. The data movement energy,  $E_{\text{Data}}$ , encompasses the energy for transferring data, including both dynamic and static power consumption. The final component,  $E_{\text{Analog}}$ , includes the energy to power the TFT, the sampling energy, and ADC energy required to convert the analog signal to scaled digital value, collectively represented as  $E_{\text{Analog}}^{\text{Read}}$ . Thus, we have  $E = E_{\text{Compute}} + E_{\text{Data}} + E_{\text{analog}}$ . For our energy calculation, we consider a spatial dataflow architecture where information (e.g., spike packets) is communicated over a Network-on-Chip (NoC) (Yan et al., 2024). This architecture is representative of modern specialized hardware such as neuromorphic chips like Loihi (Lines et al., 2018) and dataflow AI accelerators like Tenstorrent (Vasiljevic et al., 2021) and Samanova (Prabhakar et al., 2022). We consider the control logic energy to be negligible as our analysis focuses on specialized accelerator designs where such overhead is minimal (Yan et al., 2024).

Thus, we model the energy consumption of our Otters-based linear projections and attention operations. We disregard the computational cost of certain operations, such as Softmax and Layer Normalization, as their contribution to the total compute is negligible compared to large-scale matrix multiplications. The energy to perform a linear projection,  $E_{\text{Opto-FC}}$ , is modeled by Equation 8.

324 The calculation is performed over a batch of size  $B$ , a sequence of length  $S$ , and for  $C_o$  output  
 325 channels. The total energy is the sum of the following components per output element:  
 326

$$328 E_{\text{Opto-FC}} = \underbrace{B \cdot S \cdot C_o}_{\text{Total Outputs}} \cdot \left( \underbrace{C_i \cdot T \cdot (s_r \cdot (E_{\text{ACC}} + E_{\text{Analog}}^{\text{Read}} + E_{\text{move}}^{\text{sparse}}) + E_{\text{leakage}})}_{\text{Spike Processing}} + T \cdot (E_{\text{CMP}} + E_{\text{threshold}}^{\text{Read}}) + \underbrace{E_{\text{binarykv}}^{\text{Write}}}_{\text{K/V Write}} \right) \quad (8)$$

$$330$$

$$331$$

$$332$$

$$333$$

$$334$$

- 335 • Computation Energy: This includes the energy for sparse accumulations. The total number  
 336 of active accumulate operations is the workload ( $C_i$ ) scaled by the average number of spikes  
 337 ( $T \cdot s_r$ ), with each operation costing  $E_{\text{ACC}}$ . Additionally, each of the  $C_o$  output neurons  
 338 performs  $T$  comparisons against its threshold, costing  $E_{\text{CMP}}$  per comparison.
- 339 • Data Movement Energy: This is composed of dynamic and static costs. Dynamic energy  
 340 ( $E_{\text{move}}^{\text{sparse}}$ ) is consumed to move spike data and is proportional to the spike rate ( $s_r$ ). Otters  
 341 paradigm requires a dynamic, step-wise decreasing threshold, which introduces additional  
 342 dynamic energy of reading operations  $E_{\text{threshold}}^{\text{Read}}$  which is need for spiking neurons. Static  
 343 energy ( $E_{\text{leakage}}$ ) accounts for constant leakage power over the time window  $T$ . After the  
 344 computation completes, an additional energy cost,  $E_{\text{binarykv}}^{\text{Write}}$ , is incurred to write the generated  
 345 binary Key and Value vectors to SRAM, as described in Section 3.2.
- 346 • Analog Energy: Each incoming spike initiates two analog operations: first, the optoelectronic  
 347 synapse emits light, and second, the decay function is sampled at a specific time  $t_k$ .  
 348 The energy for both the light emission and the sampling event is calculated by integrating  
 349 the instantaneous power ( $P = V \cdot I$ ) over the duration of each respective operation. For the  
 350 readout circuitry, including the amplifier and the look-up-table, we adopt the energy values  
 351 of a successive approximation register-assisted pipelined ADC (Su et al., 2023). The total  
 352 energy consumed in this process is denoted  $E_{\text{Analog}}^{\text{Read}}$  per spike.

353 The energy model for attention score calculation,  $E_{\text{Opto-score}}$ , is analogous to the linear projection,  
 354 with two key differences which lies in the outer dimensions and an additional data movement cost for  
 355 reading the binary Key (or Value) vector from SRAM to determine whether the sampled membrane  
 356 potential should be added to or subtracted from the accumulator, showing in Appendix A.3.

## 358 4 RESULTS

360 In this section, we evaluate Otters on seven datasets from the GLUE benchmark. We compare its  
 361 performance against both standard QNN and SNN baselines, using BERT<sub>base</sub> as the teacher model  
 362 for knowledge distillation. We further provide a detailed analysis of the model’s energy efficiency  
 363 and robustness. All experiments were conducted on three NVIDIA A100 GPUs with a fixed 4-bit  
 364 simulation window size recommended by Sorbet (Tang et al., 2025) (In our setting, it is equal to  
 365 timestep  $T = 15$ ). The training process of Otters is shown in Appendix A.5 and the description of  
 366 dataset we adapted is shown in Appendix A.6.

### 367 4.1 GLUE BENCHMARK PERFORMANCE

369 As shown in Table 1, Otters achieves SOTA results among SNNs across all seven evaluated GLUE  
 370 tasks, consistently outperforms larger and more complex SNN models like SpikingBERT and  
 371 SpikeLM. For example, Otters surpasses existing SNNs and achieve an accuracy of 68.95% on  
 372 RTE and 91.28% on SST-2. The average accuracy for Otters is 83.22%, which is 3.42% and 2.98%  
 373 higher than Sorbet and SpikeLM, respectively.

### 375 4.2 ENERGY EFFICIENCY

377 We analyzed the energy consumption of Otters on the SST-2 dataset, comparing it against full-  
 378 precision and quantized BERT models we converted from, as well as SOTA 1-bit SNNs. The 1-bit

378  
 379 Table 1: Performance comparison on the GLUE benchmark. All scores are accuracy, except for  
 380 STS-B (Pearson correlation). “\*” indicates that the model size was not reported in the original  
 381 paper. **Bold** indicates the best performance among SNN models. Only Otters quantizes KV to 1 bit.  
 382

Model	Size	QQP	MNLI-m	SST-2	QNLI	RTE	MRPC	STS-B	Average
BERT <sub>base</sub> (Devlin et al., 2019)	418M	91.3	84.7	93.3	91.7	72.6	88.2	89.4	87.31
DistilBERT (Sanh, 2019)	207M	88.5	82.2	91.3	89.2	59.9	87.5	86.9	83.64
TinyBERT <sub>6</sub> (Jiao et al., 2020)	207M	-	84.6	93.1	90.4	70.0	87.3	83.7	84.85
Q2BERT (Zhang et al., 2020)	43.0M	67.0	47.2	80.6	61.3	52.7	68.4	4.4	54.51
BiT (Liu et al., 2022)	13.4M	82.9	77.1	87.7	85.7	58.8	79.7	71.1	77.57
SpikingFormer (Zhou et al., 2023)	*	83.8	67.8	82.7	74.6	58.8	74.0	72.3	73.43
SpikingBERT (Bal & Sengupta, 2024)	50M	86.8	78.1	88.2	85.2	66.1	79.2	82.2	80.83
SpikeLM (Xing et al., 2024b)	*	87.9	76.0	86.5	84.9	65.3	78.7	84.3	80.51
1-bit SpikeLM (Xing et al., 2024b)	*	87.2	74.9	86.6	84.5	65.7	78.9	83.9	80.24
1-bit Sorbet (Tang et al., 2025)	13.4M	86.5	77.3	90.4	86.1	60.3	79.9	78.1	79.80
<b>Otters (Ours)</b>	13.4M	<b>87.67</b>	<b>78.50</b>	<b>91.28</b>	<b>86.42</b>	<b>68.95</b>	<b>84.56</b>	<b>85.19</b>	<b>83.22</b>

392  
 393 **quantized BERT is the QNN Otters converted from which sharing the same structure and parame-**  
 394 **ters.** As detailed in Table 2, Otters consumes only 4.06 mJ per inference for one attention block.  
 395 This represents a  $41.36\times$  energy saving compared to the full BERT<sub>base</sub> model and a  $2.72\times$  efficient  
 396 compared to the 1-bit quantized BERT. Otters is also more efficient than previous SNNs, taking  
 397  $3.04\times$  energy saving of Sorbet and  $1.77\times$  of SpikingLM.

398 Appendix A.3 provides the full energy equation, detailed measurements for all compared models,  
 399 and an ablation study comparing traditional TTFS with Otters. All energy figures include com-  
 400 pute, data movement, and static components. In the same appendix section, we provide a detailed  
 401 breakdown of the energy consumption in Otters to clarify the contribution of each component.

402 Table 2: Energy consumption analysis on the SST-2 dataset. Energy is reported for each FC layer  
 403 (QKV linear projections), each QKV self-attention score calculation, and the total sum per inference.  
 404 The Energy Ratio is Energy(Full BERT) / Energy(Model) ( $\uparrow$  higher is better).

Model	FC (mJ)	QKV (mJ)	Total (mJ)	Energy Ratio( $\uparrow$ )
Full BERT (Devlin et al., 2019)	50.35	8.41	167.92	1.00x
1-bit Quantized BERT	3.31	0.55	11.03	15.2x
Sorbet (Tang et al., 2025)	3.39	1.08	12.34	13.61x
SpikingBERT (Bal & Sengupta, 2024)	6.37	2.05	23.22	7.23x
SpikingLM (Xing et al., 2024b)	2.09	0.46	7.2	23.32x
Otters (4bit kv)	<b>1.14</b>	<b>0.53</b>	<b>4.49</b>	<b>37.40x</b>
<b>Otters (1bit kv)</b>	<b>1.14</b>	<b>0.33</b>	<b>4.06</b>	<b>41.36x</b>

### 4.3 EFFECT OF KV CACHE QUANTIZATION

416 To further optimize energy, we explored the impact of quantizing the Key and Value projections  
 417 in the self-attention mechanism. Table 3 shows that reducing the KV precision from 4-bit to 1-  
 418 bit (Otters-1bitkv) yields a 10% reduction in total energy consumption (from 4.49 mJ to 4.06 mJ).  
 419 This energy saving comes at the cost of 0.23% drop in accuracy on SST-2, demonstrating a highly  
 420 favorable trade-off between efficiency and performance.

421 Table 3: Impact of KV quantization on energy and accuracy on SST-2.

Model	Energy (mJ)			Accuracy (%)
	FC	QKV	Total	
Otters-4bitkv	1.14	0.53	4.49	91.51
Otters-1bitkv	1.14	0.33	4.06	91.28

### 4.4 ROBUSTNESS DISCUSSION TO HARDWARE PARAMETER VARIATIONS

429 The practical deployment of the Otters paradigm hinges on the assumption that the physical decay  
 430 characteristics of all optoelectronic synapses are uniform. However, analog hardware is inevitably

subject to device-to-device variability from the fabrication process, which is a significant challenge for large-scale integration (Garg et al., 2022). Such inherent hardware noise can corrupt the precise time-to-value mapping that underpins our conversion method. To evaluate robustness against hardware variability (Fagbohungbe & Qian, 2021; Xuan & Narayanan, 2022; Su et al., 2024), we injected zero-mean standard deviation Gaussian noise, which is commonly used to simulate and represent hardware noise, into the physical decay function,  $O(t)$ , and its parameters,  $\tau$  and  $\beta$ . The injected noise is proportional to parameter magnitude: at level  $k$ , each parameter  $p$  is scaled as  $p \leftarrow p(1 \pm k)$ . As shown in Table 4, the baseline Otters model can tolerate about 5% total output  $O(t)$  difference with minimal accuracy impact and remains robust.

To keep improving the robustness, we propose Hardware-Aware Training (HAT), a method that builds robustness by simulating hardware non-idealities during training. We introduce two variants, HAT<sup>1</sup> and HAT<sup>2</sup>, by injecting 10% and 20% Gaussian noise, respectively, into the QNN’s activations (see Eq. 7). As shown in Table 4, both HAT settings improve noise resilience. The HAT<sup>2</sup> model maintains a stable accuracy of 80.8% even under a 20% noise level. HAT<sup>2</sup>, trained with more noise, excels in high-noise regimes, whereas HAT<sup>1</sup> achieves higher accuracy in low-noise conditions while still substantially outperforming the baseline (e.g., a 11.5% accuracy gain with 12% noise in  $O(t)$ ). Thus, HAT-trained models trade a minor drop in peak accuracy for a significant increase in resilience against hardware noise. This demonstrates that the model can be regularized to generalize across a range of hardware imperfections. Consequently, the HAT noise level can be tuned to the manufacturing tolerances of a specific hardware platform, ensuring reliable real-world performance and validating the Otters paradigm as a robust and practical approach.

Table 4: Noise Robustness in Physical Decay Function. **Bold** indicates best performance per noise level within each component group. Results: mean  $\pm$  std over 3 runs.

Method	Gaussian Noise Level				
	Full Function $O(t)$ Experiments				
$O(t)$	0.04	0.08	0.12	0.16	0.20
Otters	<b>89.9 <math>\pm</math> 0.8</b>	86.1 $\pm$ 0.8	73.8 $\pm$ 0.9	58.0 $\pm$ 0.8	53.3 $\pm$ 0.4
Otters+HAT <sup>1</sup>	89.3 $\pm$ 0.5	<b>89.0 <math>\pm</math> 0.6</b>	85.3 $\pm$ 0.6	76.5 $\pm$ 0.4	61.0 $\pm$ 0.8
Otters+HAT <sup>2</sup>	87.4 $\pm$ 0.5	87.2 $\pm$ 0.7	<b>85.9 <math>\pm</math> 0.7</b>	<b>85.2 <math>\pm</math> 0.7</b>	<b>80.8 <math>\pm</math> 0.3</b>
Parameter $\beta$ Experiments					
$\beta$	0.01	0.02	0.03	0.04	0.05
Otters	<b>90.2 <math>\pm</math> 0.1</b>	<b>89.5 <math>\pm</math> 0.1</b>	87.5 $\pm$ 1.8	79.2 $\pm$ 3.4	72.5 $\pm$ 1.4
Otters+HAT <sup>1</sup>	89.6 $\pm$ 0.1	89.2 $\pm$ 0.3	<b>89.1 <math>\pm</math> 0.4</b>	<b>87.7 <math>\pm</math> 1.2</b>	80.6 $\pm$ 2.8
Otters+HAT <sup>2</sup>	87.8 $\pm$ 0.7	88.1 $\pm$ 0.4	87.4 $\pm$ 1.0	85.5 $\pm$ 1.1	<b>83.8 <math>\pm</math> 0.5</b>
Parameters $\tau$ Experiments					
$\tau$	0.10	0.20	0.30	0.40	0.50
Otters	<b>90.3 <math>\pm</math> 0.1</b>	<b>90.1 <math>\pm</math> 0.5</b>	87.0 $\pm$ 1.7	75.0 $\pm$ 4.1	67.5 $\pm$ 4.8
Otters+HAT <sup>1</sup>	89.6 $\pm$ 0.5	89.3 $\pm$ 1.2	<b>88.2 <math>\pm</math> 0.7</b>	<b>88.2 <math>\pm</math> 1.0</b>	76.1 $\pm$ 2.8
Otters+HAT <sup>2</sup>	87.8 $\pm$ 0.6	87.7 $\pm$ 0.8	87.1 $\pm$ 0.6	87.2 $\pm$ 0.3	<b>83.0 <math>\pm</math> 1.4</b>

## 5 DISCUSSION AND FUTURE WORKS

To make SNNs more energy-efficient, Otters focuses on hardware-software co-design to optimize a core computing operation. We replace the temporal decay function and its following multiplication by sampling the natural decay of an oxide optoelectronic synapse. This shifts the computation from digital to analog for a more energy-efficient computing method. However, at the same time, many related works are also working toward better energy efficiency for SNNs, but from another direction, such as algorithmic and architectural improvements. These methods, including QKFormer, SSSA, and A<sup>2</sup>OS<sup>2</sup>A, optimize the spiking attention mechanism from  $O(N^2)$  to linear complexity (linear-attention SNNs) (Zhou et al., 2024; Wang et al., 2025b; Guo et al., 2025). These two directions are not in conflict. They are complementary and solve different parts of the problem. Future work includes designing a linear attention mechanism based on the Otters spiking neuron to make energy use even more efficient.

486 We further discuss the hardware scale. The  $\text{In}_2\text{O}_3$  optoelectronic synapse in our prototype has an  
 487 effective area of about  $0.012 \text{ mm}^2$  with a channel length of  $30 \mu\text{m}$ . This size is mainly due to  
 488 the precision limits of our fabrication equipment and does not represent the scaling limits of  $\text{In}_2\text{O}_3$   
 489 technology. Since the goal of this paper is to validate the optoelectronic TTFS mechanism, we did  
 490 not focus on device size optimization. However, recent work has demonstrated  $\text{In}_2\text{O}_3$  transistors  
 491 with channel lengths down to  $40 \text{ nm}$  (Si et al., 2021), showing that the device area can be reduced  
 492 by nearly three orders of magnitude. Additionally, several studies show that oxide devices can  
 493 be integrated in 3D stacked layers, providing another path to further reduce the effective area per  
 494 synapse (Tang et al., 2022; Yuvaraja et al., 2024; Kwak et al., 2024). With the TTFS mechanism  
 495 verified, we plan to focus on device scaling in future work. We also note that the device count can be  
 496 reduced by device sharing. For example, consider a Q-projection layer with input channels  $C_i$  and  
 497 output channels  $C_o$ . If every weight required one device, the layer would need  $O(C_i \times C_o)$  devices.  
 498 In the Otters setting, this number would reach  $10^6$ – $10^7$ , which is clearly not practical. However,  
 499 in our setting (introduced in Section 3.3), all weights are quantized to 1-bit. This means the decay  
 500 function is identical for the entire layer, making it possible to share the  $\text{In}_2\text{O}_3$  device. In the best  
 501 case, one FC layer can reuse just one physical device. Thus, a single BERT block would require  
 502 about 8 devices, resulting in a total area of  $0.096 \text{ mm}^2$ : 6 for the self-attention module (projections  
 503 of Q, K, V, their multiplication and output) and 2 for the feed-forward module. (In real systems,  
 504 the number of devices might be higher, and sharing may be limited by architecture and compiler  
 505 constraints.) The next step of this work is to design an architecture that increases this device reuse  
 506 to further reduce the chip area.

## 6 CONCLUSION

509 This paper introduces Otters, a new paradigm for energy-efficient neuromorphic computing that  
 510 challenges this digital-centric approach. Through a hardware-software co-design, we repurpose  
 511 the natural signal decay of a custom-fabricated optoelectronic synapse, transforming this physical  
 512 phenomenon into a computational method. This allows us to eliminate the costly decay function  
 513 evaluation steps inherent in traditional TTFS, fusing computation and memory into the physical  
 514 process. To deploy this paradigm in complex architectures like the Transformer, we developed a  
 515 QNN-to-SNN conversion algorithm that circumvents the challenges of direct SNN training. The Otters  
 516 model achieves state-of-the-art accuracy across seven GLUE benchmark datasets among SNNs,  
 517 while simultaneously delivering a  $1.77\times$  improvement in energy efficiency over previous leading  
 518 spiking models. By directly harnessing fundamental device physics for computation, this work  
 519 demonstrates a new path to a more energy-efficient neuromorphic computing design.

520  
 521  
 522  
 523  
 524  
 525  
 526  
 527  
 528  
 529  
 530  
 531  
 532  
 533  
 534  
 535  
 536  
 537  
 538  
 539

540 REFERENCES  
541

542 BS Ajay, Madhav Rao, et al. Mc-qdsnn: Quantized deep evolutionary snn with multi-dendritic  
543 compartment neurons for stress detection using physiological signals. *IEEE Transactions on*  
544 *Computer-Aided Design of Integrated Circuits and Systems*, 2024.

545 Bashayr Alqahtani, Hanrui Li, Abdul Momin Syed, and Nazek El-Atab. From light sensing to  
546 adaptive learning: hafnium diselenide reconfigurable memcapacitive devices in neuromorphic  
547 computing. *Light: Science & Applications*, 14(1):30, 2025.

548 Zhenyu Bai, Pranav Dangi, Rohan Juneja, Zhaoying Li, Zhanglu Yan, Huiying Lan, and Tulika  
549 Mitra. A data-driven dynamic execution orchestration architecture. *International Conference on*  
550 *Architectural Support for Programming Languages and Operating Systems (ASPLOS)*, 2025.

551 Malyaban Bal and Abhronil Sengupta. Spikingbert: Distilling bert to train spiking language models  
552 using implicit differentiation. In *Proceedings of the AAAI conference on artificial intelligence*,  
553 volume 38, pp. 10998–11006, 2024.

554 Kaiwei Che, Wei Fang, Zhengyu Ma, Yifan Huang, Peng Xue, Li Yuan, Timothée Masquelier,  
555 and Yonghong Tian. Efficiently training time-to-first-spike spiking neural networks from scratch.  
556 *arXiv preprint arXiv:2410.23619*, 2024a.

557 Kaiwei Che, Wei Fang, Zhengyu Ma, Li Yuan, Timothée Masquelier, and Yonghong Tian. Ettfs:  
558 An efficient training framework for time-to-first-spike neuron. *arXiv e-prints*, pp. arXiv-2410,  
559 2024b.

560 Manon Dampfhofer, Thomas Mesquida, Alexandre Valentian, and Lorena Anghel. Are snns re-  
561 ally more energy-efficient than anns? an in-depth hardware-aware study. *IEEE Transactions on*  
562 *Emerging Topics in Computational Intelligence*, 7(3):731–741, 2022.

563 Jacob Devlin, Ming-Wei Chang, Kenton Lee, and Kristina Toutanova. Bert: Pre-training of deep  
564 bidirectional transformers for language understanding. In *Proceedings of the 2019 conference*  
565 *of the North American chapter of the association for computational linguistics: human language*  
566 *technologies*, volume 1 (long and short papers), pp. 4171–4186, 2019.

567 Omobayode Fagbohungbe and Lijun Qian. Benchmarking inference performance of deep learning  
568 models on analog devices. In *2021 International Joint Conference on Neural Networks (IJCNN)*,  
569 pp. 1–9. IEEE, 2021.

570 Sahaj Garg, Joe Lou, Anirudh Jain, Zhimu Guo, Bhavin J Shastri, and Mitchell Nahmias. Dynamic  
571 precision analog computing for neural networks. *IEEE Journal of Selected Topics in Quantum*  
572 *Electronics*, 29(2: Optical Computing):1–12, 2022.

573 Yufei Guo, Xiaode Liu, Yuanpei Chen, Weihang Peng, Yuhan Zhang, and Zhe Ma. Spiking trans-  
574 former: Introducing accurate addition-only spiking self-attention for transformer. In *Proceedings*  
575 *of the Computer Vision and Pattern Recognition Conference*, pp. 24398–24408, 2025.

576 Mark Horowitz. 1.1 computing’s energy problem (and what we can do about it). In *2014 IEEE*  
577 *international solid-state circuits conference digest of technical papers (ISSCC)*, pp. 10–14. IEEE,  
578 2014.

579 Nidhal Jegham, Marwan Abdelatti, Lassad Elmoubarki, and Abdeltawab Hendawi. How hun-  
580 gry is ai? benchmarking energy, water, and carbon footprint of llm inference. *arXiv preprint*  
581 *arXiv:2505.09598*, 2025.

582 Xiaoqi Jiao, Yichun Yin, Lifeng Shang, Xin Jiang, Xiao Chen, Linlin Li, Fang Wang, and Qun Liu.  
583 Tinybert: Distilling bert for natural language understanding. In *Findings of the Association for*  
584 *Computational Linguistics: EMNLP 2020*, pp. 4163–4174, 2020.

585 Jungyoun Kwak, Gihun Choe, Junmo Lee, and Shimeng Yu. Monolithic 3d transposable 3t embed-  
586 ded dram with back-end-of-line oxide channel transistor. In *2024 IEEE International Symposium*  
587 *on Circuits and Systems (ISCAS)*, pp. 1–5. IEEE, 2024.

594 Dingwei Li, Yitong Chen, Huihui Ren, Yingjie Tang, Siyu Zhang, Yan Wang, Lixiang Xing,  
 595 Qi Huang, Lei Meng, and Bowen Zhu. An active-matrix synaptic phototransistor array for in-  
 596 sensor spectral processing. *Advanced Science*, 11(39):2406401, 2024a.

597

598 Dingwei Li, Guolei Liu, Fanfan Li, Huihui Ren, Yingjie Tang, Yitong Chen, Yan Wang, Rui Wang,  
 599 Saisai Wang, Lixiang Xing, et al. Double-opponent spiking neuron array with orientation selec-  
 600 tivity for encoding and spatial-chromatic processing. *Science Advances*, 11(7):eabd3584, 2025.

601

602 Fanfan Li, Dingwei Li, Chuanqing Wang, Guolei Liu, Rui Wang, Huihui Ren, Yingjie Tang, Yan  
 603 Wang, Yitong Chen, Kun Liang, et al. An artificial visual neuron with multiplexed rate and  
 604 time-to-first-spike coding. *Nature Communications*, 15(1):3689, 2024b.

605

606 Kun Liang, Rui Wang, Huihui Ren, Dingwei Li, Yingjie Tang, Yan Wang, Yitong Chen, Chunyan  
 607 Song, Fanfan Li, Guolei Liu, et al. Printable coffee-ring structures for highly uniform all-oxide  
 608 optoelectronic synaptic transistors. *Advanced Optical Materials*, 10(24):2201754, 2022.

609

610 Zheng Lin, Guanqiao Qu, Qiyuan Chen, Xianhao Chen, Zhe Chen, and Kaibin Huang. Pushing  
 611 large language models to the 6g edge: Vision, challenges, and opportunities. *arXiv preprint*  
 612 *arXiv:2309.16739*, 2023.

613

614 Andrew Lines, Prasad Joshi, Ruokun Liu, Steve McCoy, Jonathan Tse, Yi-Hsin Weng, and Mike  
 615 Davies. Loihi asynchronous neuromorphic research chip. *Energy*, 10(15):10–1109, 2018.

616

617 Fuqiang Liu and Chenchen Liu. Towards accurate and high-speed spiking neuromorphic sys-  
 618 tems with data quantization-aware deep networks. In *Proceedings of the 55th Annual Design  
 619 Automation Conference*, pp. 1–6, 2018.

620

621 Zechun Liu, Barlas Oguz, Aasish Pappu, Lin Xiao, Scott Yih, Meng Li, Raghuraman Krishnamoorti,  
 622 and Yashar Mehdad. Bit: Robustly binarized multi-distilled transformer. *Advances in neural  
 623 information processing systems*, 35:14303–14316, 2022.

624

625 Raghu Prabhakar, Sumti Jairath, and Jinuk Luke Shin. Sambanova sn10 rdu: A 7nm dataflow ar-  
 626 chitecture to accelerate software 2.0. In *2022 IEEE International Solid-State Circuits Conference  
 627 (ISSCC)*, volume 65, pp. 350–352. IEEE, 2022.

628

629 V Sanh. Distilbert, a distilled version of bert: smaller, faster, cheaper and lighter. In *Proceedings of  
 630 Thirty-third Conference on Neural Information Processing Systems (NIPS2019)*, 2019.

631

632 Jialin Shi, Jiansheng Jie, Wei Deng, Gan Luo, Xiaochen Fang, Yanling Xiao, Yujian Zhang, Xiujuan  
 633 Zhang, and Xiaohong Zhang. A fully solution-printed photosynaptic transistor array with ultralow  
 634 energy consumption for artificial-vision neural networks. *Advanced Materials*, 34(18):2200380,  
 635 2022.

636

637 Mengwei Si, Zehao Lin, Zhizhong Chen, and Peide D Ye. High-performance atomic-layer-  
 638 deposited indium oxide 3-d transistors and integrated circuits for monolithic 3-d integration. *IEEE  
 639 Transactions on Electron Devices*, 68(12):6605–6609, 2021.

640

641 Qing Su, Dawei Li, Xuan Guo, Heng Zhang, Ben He, Hanbo Jia, Danyu Wu, and Xinyu Liu. A  
 642 5.3-fj/conv.-step pipelined-sar adc with resistance assisted two-stage dynamic amplifier based on  
 643 gm-unit. In *2023 8th International Conference on Integrated Circuits and Microsystems (ICICM)*,  
 644 pp. 322–325. IEEE, 2023.

645

646 Rui Su, Dunbao Chen, Weiming Cheng, Ruizi Xiao, Yuheng Deng, Yufeng Duan, Yi Li, Lei Ye,  
 647 Hongyu An, Jingping Xu, et al. Oxygen vacancy compensation-induced analog resistive switch-  
 648 ing in the srfeo3-  $\delta$ /nb: Srtio3 epitaxial heterojunction for noise-tolerant high-precision image  
 649 recognition. *ACS Applied Materials & Interfaces*, 16(40):54115–54128, 2024.

650

651 Kaiwen Tang, Zhanglu Yan, and Weng-Fai Wong. Sorbet: A neuromorphic hardware-compatible  
 652 transformer-based spiking language model. In *Forty-second International Conference on Machine  
 653 Learning*, 2025.

648 W Tang, Z Wang, Z Lin, L Feng, Z Liu, X Li, PD Ye, X Guo, and M Si. Monolithic 3d integration  
 649 of vertically stacked cmos devices and circuits with high-mobility atomic-layer-deposited in 2 o 3  
 650 n-fet and polycrystalline si p-fet: Achieving large noise margin and high voltage gain of 134 v/v.  
 651 In 2022 International Electron Devices Meeting (IEDM), pp. 483–486. IEEE, 2022.

652  
 653 Jasmina Vasiljevic, Ljubisa Bajic, Davor Capalija, Stanislav Sokorac, Dragoljub Ignjatovic, Lejla  
 654 Bajic, Milos Trajkovic, Ivan Hamer, Ivan Matosevic, Aleksandar Cejkov, et al. Compute substrate  
 655 for software 2.0. IEEE micro, 41(2):50–55, 2021.

656 Jingya Wang, Xin Deng, Wenjie Wei, Dehao Zhang, Shuai Wang, Qian Sun, Jieyuan Zhang, Han-  
 657 wen Liu, Ning Xie, and Malu Zhang. Training-free ann-to-snn conversion for high-performance  
 658 spiking transformer. arXiv preprint arXiv:2508.07710, 2025a.

659  
 660 Shuai Wang, Malu Zhang, Dehao Zhang, Ammar Belatreche, Yichen Xiao, Yu Liang, Yimeng Shan,  
 661 Qian Sun, Enqi Zhang, and Yang Yang. Spiking vision transformer with saccadic attention. arXiv  
 662 preprint arXiv:2502.12677, 2025b.

663 Xiaoyu Wang, Yixin Zong, Duanyang Liu, Juehan Yang, and Zhongming Wei. Advanced optoelec-  
 664 tronic devices for neuromorphic analog based on low-dimensional semiconductors. Advanced  
 665 Functional Materials, 33(15):2213894, 2023.

666  
 667 Yun Wang, Yanfang Zha, Chunxiong Bao, Fengrui Hu, Yunsong Di, Cihui Liu, Fangjian Xing,  
 668 Xingyuan Xu, Xiaoming Wen, Zhixing Gan, et al. Monolithic 2d perovskites enabled artificial  
 669 photonic synapses for neuromorphic vision sensors. Advanced Materials, 36(18):2311524, 2024.

670 Wenjie Wei, Malu Zhang, Hong Qu, Ammar Belatreche, Jian Zhang, and Hong Chen. Temporal-  
 671 coded spiking neural networks with dynamic firing threshold: Learning with event-driven back-  
 672 propagation. In Proceedings of the IEEE/CVF international conference on computer vision, pp.  
 673 10552–10562, 2023.

674  
 675 Pengshan Xie, Dengji Li, SenPo Yip, and Johnny C Ho. Emerging optoelectronic artificial synapses  
 676 and memristors based on low-dimensional nanomaterials. Applied Physics Reviews, 11(1), 2024.

677 Xingrun Xing, Boyan Gao, Zheng Zhang, David A Clifton, Shitao Xiao, Li Du, Guoqi Li, and Jiajun  
 678 Zhang. Spikellm: Scaling up spiking neural network to large language models via saliency-based  
 679 spiking. arXiv preprint arXiv:2407.04752, 2024a.

680  
 681 Xingrun Xing, Zheng Zhang, Ziyi Ni, Shitao Xiao, Yiming Ju, Siqi Fan, Yequan Wang, Jiajun  
 682 Zhang, and Guoqi Li. Spikelm: Towards general spike-driven language modeling via elastic  
 683 bi-spiking mechanisms. In Forty-first International Conference on Machine Learning, 2024b.

684 Ziwei Xuan and Krishna Narayanan. Low-delay analog joint source-channel coding with deep  
 685 learning. IEEE Transactions on Communications, 71(1):40–51, 2022.

686  
 687 Zhanglu Yan, Zhenyu Bai, and Weng-Fai Wong. Reconsidering the energy efficiency of spiking  
 688 neural networks. arXiv preprint arXiv:2409.08290, 2024.

689 Miao Yu, Tingting Xiang, Srivatsa P, Kyle Timothy Ng Chu, Burin Amornpaisanon, Yaswanth  
 690 Tavva, Venkata Pavan Kumar Miriyala, and Trevor E Carlson. A tfs-based energy and utilization  
 691 efficient neuromorphic cnn accelerator. Frontiers in Neuroscience, 17:1121592, 2023.

692  
 693 Saravanan Yuvaraja, Hendrik Faber, Mritunjay Kumar, Na Xiao, Glen Isaac Maciel García, Xiao  
 694 Tang, Thomas D Anthopoulos, and Xiaohang Li. Three-dimensional integrated metal-oxide tran-  
 695 sistor. Nature Electronics, 7(9):768–776, 2024.

696 Wei Zhang, Lu Hou, Yichun Yin, Lifeng Shang, Xiao Chen, Xin Jiang, and Qun Liu. Ternary-  
 697 bert: Distillation-aware ultra-low bit bert. In Proceedings of the 2020 Conference on Empirical  
 698 Methods in Natural Language Processing (EMNLP), pp. 509–521, 2020.

699  
 700 Lusen Zhao, Zihan Huang, Jianhao Ding, and Zhaofei Yu. Ttfsformer: A tfs-based lossless con-  
 701 version of spiking transformer. In Forty-second International Conference on Machine Learning,  
 2025.

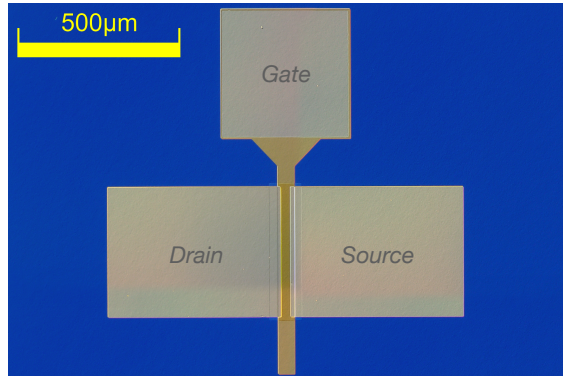
702 Chenlin Zhou, Liutao Yu, Zhaokun Zhou, Zhengyu Ma, Han Zhang, Huihui Zhou, and Yonghong  
703 Tian. Spikingformer: Spike-driven residual learning for transformer-based spiking neural net-  
704 work. [arXiv preprint arXiv:2304.11954](https://arxiv.org/abs/2304.11954), 2023.

705 Chenlin Zhou, Han Zhang, Zhaokun Zhou, Liutao Yu, Liwei Huang, Xiaopeng Fan, Li Yuan,  
706 Zhengyu Ma, Huihui Zhou, and Yonghong Tian. Qkformer: Hierarchical spiking transformer  
707 using qk attention. [Advances in Neural Information Processing Systems](https://proceedings.neurips.cc/paper/2024/file/3713074-13098.pdf), 37:13074–13098, 2024.

709  
710  
711  
712  
713  
714  
715  
716  
717  
718  
719  
720  
721  
722  
723  
724  
725  
726  
727  
728  
729  
730  
731  
732  
733  
734  
735  
736  
737  
738  
739  
740  
741  
742  
743  
744  
745  
746  
747  
748  
749  
750  
751  
752  
753  
754  
755

756 A APPENDIX  
757758 A.1 FABRICATED  $\text{In}_2\text{O}_3$  TFTS  
759

760 To prepare the indium oxide thin-film transistors ( $\text{In}_2\text{O}_3$  TFTs), indium nitrate was first dissolved  
761 in a mixed solvent of 2-methoxyethanol (2-ME), acetylacetone (AcAc), and ammonium hydroxide  
762 ( $\text{NH}_3 \cdot \text{H}_2\text{O}$ ) to form a precursor solution, which was stirred overnight to ensure complete dissolu-  
763 tion and coordination. Subsequently, gate electrodes were fabricated on a silicon substrate coated  
764 with a  $\text{SiO}_2$  insulating layer, followed by sequential deposition of 8 nm chromium and 50 nm gold  
765 via electron-beam evaporation. A 30 nm-thick  $\text{Al}_2\text{O}_3$  dielectric layer was then uniformly deposited  
766 over the substrate using atomic layer deposition (ALD). The  $\text{In}_2\text{O}_3$  precursor solution was spin-  
767 coated onto the dielectric surface, after which the channel regions were defined through standard  
768 photolithography, and the unprotected areas were removed by hydrochloric acid wet etching. The  
769 films were annealed in air at 300 °C for 1 hour to enhance crystallinity and improve film quality.  
770 Portions of the  $\text{Al}_2\text{O}_3$  layer were subsequently etched to expose selected regions of the gate elec-  
771 trodes. Finally, source and drain electrodes, along with interconnects, were patterned and metallized  
772 with an additional 8 nm chromium and 50 nm gold layer via electron-beam evaporation. The indium  
773 oxide thin-film transistor was characterized under a gate bias of 0 V and a drain bias of 5 mV. Upon  
774 405 nm laser illumination, oxygen vacancies in the channel layer were photoionized, generating free  
775 electrons and thereby enhancing the channel conductivity.

776 (a) Optical microscope  
777778 (b) OTTERS under optical microscope  
779780 Figure 5: Details design of OTTERS  
781

782 Regarding integration with state-of-the-art digital hardware, recent studies show that  $\text{In}_2\text{O}_3$  TFTs  
783 are compatible with 3D stacking on CMOS chips. This is because they have a low thermal budget  
784 ( $\leq 300$  °C) and good uniformity (Tang et al., 2022). This provides a practical path for vertical  
785 integration. However, several challenges remain, such as managing wire density in stacked layers,  
786 aligning the photodetectors/TFT layers with metal layers, and handling device variability in large  
787 arrays.

788 A.2 PROOF FOR PROPOSITION 1  
789800 A.2.1 INTEGRATION PHASE EQUIVALENCE  
801

802 The foundation of the proof lies in the relationship between the QNN’s discrete value and the SNN’s  
803 spike time. From Section 3.3, we know that the QNN output activation from the previous layer is  
804  $x_{q,i}^{l-1} = \alpha^{l-1} \cdot q_i^{l-1}$ , where  $q_i^{l-1}$  is the integer value:

$$805 \quad q_i^{l-1} = \text{Clip} \left( \left\lfloor \frac{a_i^{l-1}}{\alpha^{l-1}} \right\rfloor, 0, T \right) \quad (9)$$

806 We define the TTFS encoding scheme such that this integer value  $q_i^{l-1}$  is represented by a single  
807 spike from neuron  $i$  at the discrete time step  $k$ :

$$808 \quad k = T - q_i^{l-1} \quad (10)$$

This encoding adheres to the TTFS principle: a larger integer value  $q_i^{l-1}$  results in a smaller time step  $k$ , signifying an earlier spike. A value of 0 corresponds to no spike within the active window, and the maximum value  $T$  corresponds to a spike at  $k = 0$ .

When a presynaptic neuron  $i$  fires at time step  $k$ , its contribution to the postsynaptic potential of neuron  $j$  is given by the *Otters* PSP function,  $\epsilon'(\cdot)$ . Using the conditions specified in Proposition 1, the normalized value produced by the decay function  $O(t)$  at time step  $t_k$  is:

$$O(t_k) = \frac{T - k}{T} \quad (11)$$

Substituting the encoding relationship from Step 1 ( $k = T - q_i^{l-1}$ ):

$$O(t_k) = \frac{T - (T - q_i^{l-1})}{T} = \frac{q_i^{l-1}}{T} \quad (12)$$

Thus we find that the normalized output of the physical decay process at the spike time  $t_k$  is directly proportional to the integer value  $q_i^{l-1}$  it is meant to encode.

The full PSP contribution from the synapse connecting  $i$  to  $j$  is the product of this normalized value and the scaling factor  $\gamma_{ij}^l$ . Using the definition of  $\gamma$  from Proposition 1:

$$\gamma_{ij}^l = w_{ij}^l \cdot \alpha^{l-1} \cdot T \quad (13)$$

The PSP is therefore:

$$\begin{aligned} \epsilon'(w_{ij}^l, t_k) &= \gamma_{ij}^l \cdot O(t_k) \\ &= (w_{ij}^l \cdot \alpha^{l-1} \cdot T) \cdot \left( \frac{q_i^{l-1}}{T} \right) \\ &= w_{ij}^l \cdot (\alpha^{l-1} \cdot q_i^{l-1}) \end{aligned} \quad (14)$$

Recognizing that  $x_{q,i}^{l-1} = \alpha^{l-1} \cdot q_i^{l-1}$ , we find:

$$\epsilon'(w_{ij}^l, t_k) = w_{ij}^l \cdot x_{q,i}^{l-1} \quad (15)$$

This shows that the contribution of a single spike in the SNN is exactly equal to the weighted input term in the QNN.

The final membrane potential  $V_j^l$  is the sum of all such PSPs from incoming spikes, plus the bias term:

$$V_j^l = \sum_i \epsilon'(w_{ij}^l, t_{\text{spike},i}^{l-1}) + b_j^l = \sum_i (w_{ij}^l \cdot x_{q,i}^{l-1}) + b_j^l \quad (16)$$

By comparing this with the definition of the QNN pre-activation from Section 1.2,

$$a_j^l = \sum_i w_{ij}^l x_{q,i}^{l-1} + b_j^l \quad (17)$$

we arrive at the desired equality:

$$V_j^l = a_j^l \quad (18)$$

### A.2.2 FIRING PHASE EQUIVALENCE

In this section, we prove that the integer value encoded by the SNN's output spike time,  $t_{\text{spike},j}^l$ , is equal to the integer value of the QNN's output,  $q_j^l$ . That is, if  $t_{\text{spike},j}^l$  corresponds to time step  $k_{\text{fire}}$ , we have:

$$T - k_{\text{fire}} = q_j^l = \text{Clip} \left( \left\lfloor \frac{a_j^l}{\alpha^l} \right\rfloor, 0, T \right) \quad (19)$$

According to the SNN model definition, the neuron fires at the earliest discrete time step  $k$  for which its potential  $V_j^l$  meets or exceeds the threshold  $\theta^l(t_k)$ .

$$V_j^l \geq \theta^l(t_k) \quad (20)$$

Substituting the result from Part I ( $V_j^l = a_j^l$ ) and the definition of the time-varying threshold from Proposition 1 ( $\theta^l(t_k) = \alpha^l \cdot (T - k)$ ), the firing condition becomes:

$$a_j^l \geq \alpha^l \cdot (T - k) \quad (21)$$

Assuming  $\alpha^l > 0$ , we can rearrange the inequality to solve for the term  $(T - k)$ , which represents the integer value that would be encoded by a spike at time step  $k$ :

$$\frac{a_j^l}{\alpha^l} \geq T - k \quad (22)$$

The threshold  $\theta^l(t_k) = \alpha^l(T - k)$  is a monotonically decreasing function of the time step  $k$ . For a fixed membrane potential  $a_j^l$ , this means that if the firing condition is met for a certain time step  $k^*$ , it will also be met for all subsequent time steps  $k > k^*$ . The TTFS firing rule dictates that the neuron fires at the first time step that satisfies the condition. This corresponds to finding the smallest integer  $k$  that satisfies the inequality (largest  $T - k$ ). By the definition of the floor function, the integer value encoded by the output spike, which is defined by our encoding scheme as  $q_{\text{out},j}^l = T - k_{\text{fire}}$ , is:

$$q_j^l = \left\lfloor \frac{a_j^l}{\alpha^l} \right\rfloor \quad (23)$$

The derivation above assumes the result of the floor function falls within the valid range of encodable integers. We now analyze the boundary conditions imposed by the finite simulation window.

- **Upper Bound (Clipping at T)** If the pre-activation  $a_j^l$  is very large such that  $\lfloor a_j^l / \alpha^l \rfloor > T$ , the condition  $a_j^l / \alpha^l \geq T - k$  will be satisfied for all  $k \in T$ . The neuron will fire at the earliest possible time step, which is  $k = 0$ . The value encoded by a spike at  $k = 0$  is  $T - 0 = T$ . This naturally implements the upper bound of the clipping function, mapping any integer value greater than  $T$  to  $T$ .
- **Lower Bound (Clipping at 0)**. If the pre-activation  $a_j^l$  is such that  $\lfloor a_j^l / \alpha^l \rfloor < 0$ , then the term  $a_j^l / \alpha^l$  is negative. Thus, the firing condition  $a_j^l / \alpha^l \geq T - k$  can never be satisfied. The neuron will not fire within the time window. The absence of a spike is interpreted as encoding the integer value 0. This naturally implements the lower bound of the clipping function.

Combining these cases, the integer value encoded by the SNN’s firing mechanism,  $q'_{\text{out},j}$ , is:

$$q'_{\text{out},j} = \text{Clip} \left( \left\lfloor \frac{a_j^l}{\alpha^l} \right\rfloor, 0, T \right) \quad (24)$$

This is identical to the definition of the QNN’s integer output,  $q_j^l$ .

### A.3 ENERGY ANALYSIS

#### A.3.1 ENERGY COMPARISON WITH RELATED WORKS

For the energy calculation in Table 2, we did not use the numbers reported in the original papers. Since energy depends heavily on batch size and sequence length, a direct comparison is often unfair. Furthermore, most related works do not account for hardware overhead, which actually dominates the total energy. Therefore, we re-calculated their energy to ensure a fair comparison. We assumed the same model size, batch size, sequence length and weight quantization level for all works.

For Transformer baselines, the energy consumption of a Full BERT (FP32) is dominated by expensive 32-bit multiply-accumulate (MAC) operations and data movement. We also compared it to a

918 Quantized BERT (INT4), which uses the same architectural settings as Otter, including 1-bit weight,  
 919 4-bit activations and a 1-bit Key-Value (KV) cache.  
 920

921 For SNNs, we used the energy equations we built for them, which depend on the spike rate ( $s_r$ ) and  
 922 the number of timesteps ( $T$ ). To match Otters' performance, we selected the most optimized settings  
 923 for the baselines (Sorbet, SpikingBERT, and SpikingLM). This resulted in spike rates of 13% for  
 924 Sorbet, 25% for SpikingBERT, and 33% for SpikingLM. We used the timestep values ( $T$ ) directly  
 925 from their original papers: 16, 16, and 4, respectively.  
 926

### 926 Full BERT (FP32)

$$927 E_{FC} = B \cdot S \cdot C_o \cdot (\gamma \cdot C_i \cdot (E_{MAC} + E_{weight}^{Read} + 32 \cdot E_{move}^{sparse}) + C_i \cdot E_{leakage} + 2E_{clamp} + E_{kv}^{write}) \quad (25)$$

$$928 E_{FC-score} = B \cdot h \cdot S^2 \cdot (d_k \cdot \gamma \cdot (E_{kv}^{Read} + E_{MAC} + 32 \cdot E_{move}^{sparse}) + d_k \cdot E_{leakage} + 2E_{clamp}) \quad (26)$$

### 929 Quantized BERT

$$931 E_{FC_q} = B \cdot S \cdot C_o \cdot (\gamma \cdot C_i \cdot (E_{MAC} + E_{weight}^{Read} + \log_2(T+1) \cdot E_{move}^{sparse}) + C_i \cdot E_{leakage} + 2E_{clamp} + E_{kv}^{write}) \quad (27)$$

$$932 E_{FC_q-score} = B \cdot h \cdot S^2 \cdot (d_k \cdot \gamma \cdot (E_{kv}^{Read} + E_{MAC} + \log_2(T+1) \cdot E_{move}^{sparse}) + d_k \cdot E_{leakage} + 2E_{clamp}) \quad (28)$$

### 934 Typical SNNs

$$935 E_{SNN-FC} = B \cdot S \cdot C_o \cdot (C_i \cdot s_r \cdot T \cdot (E_{ACC} + E_{weight}^{Read} + E_{move}^{sparse}) + C_i \cdot T \cdot E_{leakage} + T \cdot (E_{CMP} + s \cdot E_{SUB}) + E_{kv}^{Write}) \quad (29)$$

$$936 E_{SNN-score} = B \cdot h \cdot S^2 \cdot (d_k \cdot s_r \cdot T \cdot (E_{kv}^{Read} + E_{ACC} + E_{move}^{sparse}) + d_k \cdot T \cdot E_{leakage} + T \cdot (E_{CMP} + s \cdot E_{SUB})) \quad (30)$$

### 939 Otters

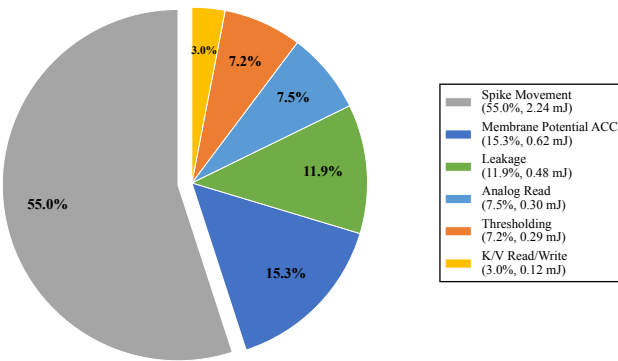
$$941 E_{Opto-FC} = \underbrace{B \cdot S \cdot C_o}_{\text{Total Outputs}} \cdot \left( \underbrace{C_i \cdot T \cdot (s_r \cdot (E_{ACC} + E_{Analog}^{Read} + E_{move}^{sparse}))}_{\text{Spike Processing}} \right. \\ 942 \left. + E_{leakage} \right) + \underbrace{T \cdot (E_{CMP} + E_{threshold}^{Read})}_{\text{Thresholding}} + \underbrace{E_{binarykv}^{Write}}_{\text{K/V Write}} \quad (31)$$

$$949 E_{Opto-score} = \underbrace{B \cdot h \cdot S^2}_{\text{Total Scores}} \cdot \left( \underbrace{d_k \cdot T \cdot (s_r \cdot (E_{ACC} + E_{Analog}^{Read} + E_{move}^{sparse} + E_{binarykv}^{Read}))}_{\text{Spike Processing}} \right. \\ 950 \left. + E_{leakage} \right) + \underbrace{T \cdot (E_{CMP} + E_{threshold}^{Read})}_{\text{Thresholding}} \quad (32)$$

955 Key differences between Otters and other typical SNNs include replacing digital weight reads with  
 956 lower-energy analog reads from the TFT ( $E_{Analog}^{Read}$ ) and, for the QKV calculation, using an energy-  
 957 efficient binary KV read ( $E_{binarykv}^{Read}$ ). The energy model is configured for a BERT-base architecture  
 958 with a batch size ( $B$ ) of 64, a sequence length ( $S$ ) of 128, and input/output channel dimensions  
 959 ( $C_i, C_o$ ) of 768. The model features 12 attention heads ( $h$ ), with a per-head dimension ( $d_k$ ) of  
 960 64. Energy costs are derived from established models. For FP32 operations, we assume that a  
 961 multiply-accumulate (MAC) consumes 4.6 pJ and a clamp operation consumes 0.9 pJ which is  
 962 from (Horowitz, 2014) cause our platform doesn't support FP calculations. For our INT4 models,  
 963 we differentiate between a 4-4-16bits MAC (0.0848 pJ) and a 1-4-16bits MAC (0.0663 pJ). The  
 964 costs for 4-16-16bits, 2-16-16bits and 1-16-16bits ACC are 0.0502 pJ, 0.0477 pJ and 0.0429 pJ,  
 965 respectively. SNN-specific operations, such as comparison and subtraction, are each modeled at  
 966 0.0502 pJ. The total energy for an analog read operation is 0.0246 pJ (0.00875 pJ for power the TFT,  
 967 1.33e-6 pJ for sampling, 0.0053 pJ for ADC including the amplifier and 0.010505 for the 4bits LUT).  
 968 The model accounts for a static leakage energy  $E_{leakage}$  of 0.002 pJ per cycle, a weight activation  
 969 (read/write) cost of 0.0985 pJ/bit, and a sparse data movement cost of 0.18 pJ per bit. All integer  
 970 compute, data movement, and memory access costs are based on measurements from a commercial  
 971 22nm process, while the floating-point compute energy (Horowitz, 2014) and ADC values (Su et al.,  
 972 2023) are taken from existing literature.

972 A.3.2 DETAILED ENERGY BREAKDOWN  
973974 Table 5 and Figure 6 detail the energy breakdown of Otters-1bitkv. Spike movement is the main  
975 energy consumer, accounting for approximately 55% of the total. The next largest contributor is  
976 membrane potential accumulation (Mem. ACC), while K/V read/write (K/V R/W) consumes the  
977 least energy.978  
979 Table 5: Energy breakdown of the Otters self-attention block (in mJ). “Mem. ACC” denotes  
980 membrane-potential accumulation; “K/V R/W” denotes key/value read/write.

Block	Compute		Data movement		Read analog	Leakage	Total
	Mem. ACC	Thresh.	Spike movement	K/V R/W			
Opto-FC	0.5611	0.1257	2.0117	0.0012	0.2744	0.4349	3.4091
Opto-qkv	0.0623	0.1676	0.2235	0.1223	0.0305	0.0483	0.6546
<b>Total</b>	<b>0.6235</b>	<b>0.2933</b>	<b>2.2352</b>	<b>0.1235</b>	<b>0.3049</b>	<b>0.4832</b>	<b>4.0637</b>

1001 Figure 6: Proportional Energy Breakdown of Otters-1bitkv.  
1002  
10031004 A.3.3 ABLATION STUDY OF SOFTMAX AND LAYER NORMALIZATION  
10051006 We initially omitted Softmax and Layer Normalization from our energy analysis, as their consump-  
1007 tion is negligible compared to the matrix multiplication operations. In this section, we present an  
1008 ablation study that accounts for these operations. We adopt the energy models from Sorbet (Tang  
1009 et al., 2025), which define the costs for Softmax as  $O(d)$  ACC,  $O(d)$  division, and  $O(d)$  exponential  
1010 operations. The same model defines LayerNorm costs as  $O(5d)$  ACC,  $O(3d)$  MAC,  $O(d)$  division,  
1011 and  $O(1)$  exponential operations. We calculated the total energy for one complete transformer block  
1012 in Figure 7, including QKV projections, attention score calculations, the attention output projection,  
1013 Softmax, Layer Normalization, and the feedforward layers (intermediate size of 3072). The results  
1014 show that Softmax and LayerNorm account for only 0.32% of the energy in the Otters block. Also,  
1015 Otters remains the most efficient method compared to related works.1016 A.3.4 ABLATION STUDY OF USING OTTERS AND TRADITIONAL TTFS METHODS  
10171018 We can group TTFS encoding into two main classes: continuous-time TTFS and quantized-time  
1019 TTFS. In other work, like TTFSFormer (Zhao et al., 2025), the time domain is continuous. This  
1020 means they pass the time-to-first-spike between layers using floating-point (FP32) values. This high-  
1021 precision FP32 number helps keep the SNN accurate after the ANN–SNN conversion. However,  
1022 comparing the energy of these continuous-time methods with our approach, which uses quantized  
1023 time, is not fair. In TTFSFormer, their main math unit (e.g., the accumulator, ACC) is FP32 and  
1024 costs about 0.9 pJ per operation, while our INT4 ACC only costs 0.05 pJ. Also, the data movement  
1025 cost grows with bit-width. This means continuous-time TTFS designs use much more memory and  
movement energy than low-bit designs.

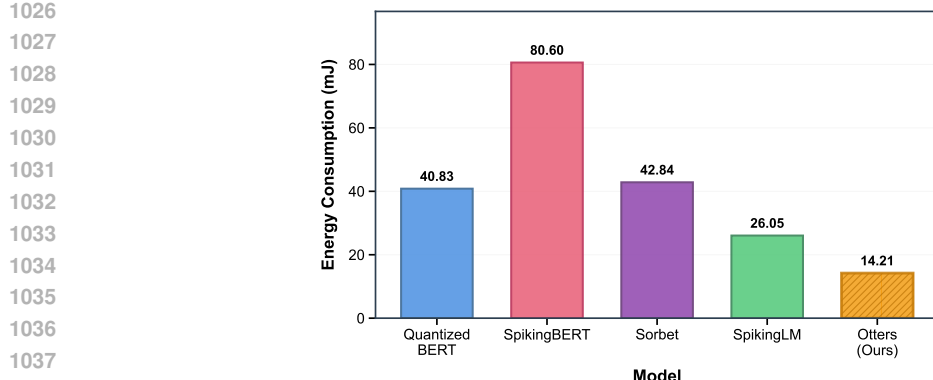


Figure 7: Energy Consumption per Transformer Block with softmax and layerNorm.

To make a fair comparison, we re-evaluated the continuous-time TTFS method in the same quantized time domain as Otters. We did this by quantizing the spike times while keeping the weights, network structure, and all other hyperparameters the same. This lets us clearly see the benefit of Otters’ analog-based computing. Traditional quantized-time TTFS requires digital encoding, additional MAC operations ( $E_{\text{encoding}} + E_{\text{MAC}}$ ), and extra weight accesses. With  $T=15$  using the simplest  $T-t$  encoding (4-4-4-bit ACC, 0.0163 pJ), traditional TTFS attention block consumes 5.12 mJ, 26.1% more energy than 1bit Otters.

#### A.4 FORWARD PROCESS OF OTTERS

The forward process is shown in Algorithm 1:

---

##### Algorithm 1 Otters Neuron Forward Pass (TTFS)

---

```

1: Inputs: Presynaptic spikes  $\{s_i^{l-1}(t)\}_{i=1}^{N_{in}}$ ; weights  $\{\gamma_{ij}^l\}_{i=1}^{N_{in}}$ ; bias  $b_j^l$ ; threshold function  $\theta^l(t)$ ; total time steps  $T$ .
2: Output: Postsynaptic spike train  $\{s_j^l(t)\}_{t=1}^T$ .
3:  $V_j \leftarrow b_j^l$  {Initialize membrane potential with bias}
4:  $s_j^l[1 : T] \leftarrow 0$  {Initialize output spike train to zeros}
5: has_fired  $\leftarrow \text{false}$ 
6: for  $t = 1, 2, \dots, T$  do
7:   for  $i = 1, 2, \dots, N_{in}$  do
8:     if  $s_i^{l-1}(t) = 1$  then
9:        $v_i \leftarrow \gamma_{ij}^l \cdot O(t)$  {Compute PSP using the physical decay function  $O(t)$ }
10:       $V_j \leftarrow V_j + v_i$  {Accumulate potential}
11:    end if
12:   end for
13:   if  $V_j \geq \theta^l(t)$  and not has_fired then
14:      $s_j^l(t) \leftarrow 1$  {Fire a spike at the current time step}
15:     has_fired  $\leftarrow \text{true}$ 
16:     break {TTFS constraint: emit at most one spike and stop}
17:   end if
18: end for
19: return  $s_j^l$ 

```

---

#### A.5 QNN TRAINING ALGORITHM

To mitigate the accuracy degradation from quantization, we employ a knowledge distillation (KD) framework for our quantization-aware training (Liu et al., 2022; Tang et al., 2025). This approach

1080  
1081  
1082  
1083  
1084  
1085  
1086  
1087  
1088  
1089  
1090  
1091  
1092  
1093  
1094  
1095  
1096  
1097  
1098  
1099  
1100  
1101  
1102  
1103  
1104  
1105  
1106  
1107  
1108  
1109  
1110  
1111  
1112  
1113  
1114  
1115  
1116  
1117  
1118  
1119  
1120  
1121  
1122  
1123  
1124  
1125  
1126  
1127  
1128  
1129  
1130  
1131  
1132  
1133  
Table 6: Task-specific training hyperparameters.

Task	Max. Seq. Length	Batch Size	Learning Rate
MNLI	128	80	$2 \times 10^{-4}$
MRPC	128	80	$5 \times 10^{-5}$
SST-2	64	80	$1 \times 10^{-4}$
STS-B	128	80	$5 \times 10^{-5}$
QQP	128	80	$2 \times 10^{-5}$
QNLI	128	80	$2 \times 10^{-4}$
RTE	128	80	$5 \times 10^{-5}$

transfers inductive biases from a pre-trained, full-precision teacher model to the quantized student network. Our training objective is a hybrid loss function that aligns both the output distributions and the intermediate representations of the student with those of the teacher. The total distillation loss  $L_{KD}$  is a weighted combination of two components: a logits distillation loss  $L_{\text{logits}}$  and a representation distillation loss  $L_{\text{reps}}$ :

$$L_{KD} = L_{\text{logits}} + \lambda L_{\text{reps}} \quad (33)$$

where  $\lambda$  is a hyperparameter that balances the two terms.

The first component,  $L_{\text{logits}}$ , is the Kullback-Leibler (KL) divergence between the teacher’s soft target distribution  $p$  and the student’s output distribution  $q$ . This loss encourages the student to learn the teacher’s predictions and its understanding of inter-class similarities.

$$L_{\text{logits}} = \text{KL}(p||q) \quad (34)$$

The second component,  $L_{\text{reps}}$ , minimizes the Mean Squared Error (MSE) between the intermediate feature representations from corresponding transformer blocks of the teacher ( $r_i^t$ ) and the student ( $r_i^s$ ). This forces the student to mimic the teacher’s internal representation structure.

$$L_{\text{reps}} = \sum_i \|r_i^t - r_i^s\|_2^2 \quad (35)$$

The student model is trained end-to-end by minimizing  $L_{KD}$  using the Adam optimizer, while the teacher model’s weights remain frozen. We use task-specific hyperparameters for training, which are detailed in Table 6. All models are trained on A100 GPUs.

## A.6 EVALUATION BENCHMARK

We evaluated our model, Otters, on seven datasets from the GLUE benchmark:

- MNLI (Multi-Genre Natural Language Inference): A large-scale, crowdsourced collection of sentence pairs annotated for textual entailment across multiple genres.
- QQP (Quora Question Pairs): A paraphrase identification task to determine if two questions from Quora are semantically equivalent.
- QNLI (Question-Answering NLI): A natural language inference task converted from the Stanford Question Answering Dataset (SQuAD), where the goal is natural language inference
- SST-2 (Stanford Sentiment Treebank): A single-sentence classification task for sentiment analysis (positive or negative) on movie reviews.
- STS-B (Semantic Textual Similarity Benchmark): A regression task to predict the degree of similarity (on a 1–5 scale) between sentence pairs drawn from news headlines, video titles, and image captions.
- RTE (Recognizing Textual Entailment): A compilation of data from several textual entailment challenges, using text from news articles and Wikipedia.
- MRPC (Microsoft Research Paraphrase Corpus): A paraphrase detection task using sentence pairs from online news sources. The dataset is imbalanced, with 68% of pairs being paraphrases.

1134  
1135

### A.7 INFERENCE TIME ANALYSIS

1136  
1137  
1138  
1139  
1140  
1141  
1142  
1143  
1144

In Otters, the inference latency is mainly determined by the duration of the optical decay function (Figure 2b in the revised manuscript). Within this time window, the SNN neuron compares its accumulated membrane potential with the dynamic threshold at each time step  $t_k$ . If the membrane potential is larger than the threshold, the neuron fires. It then samples the value from the thin-film transistor and adds it to the next neuron’s membrane potential. Once the decay period finishes, the next layer is ready to start. Thus, in theory, the computation for one layer is completed within a single time window. Taking a Transformer block as an example, the calculation requires roughly 8 optical cycles: 6 cycles for the Self-Attention module (projections of Q, K, V, their multiplication and output) and 2 cycles for the Feedforward module.

1145  
1146  
1147  
1148  
1149  
1150

In our current measurements, the transient optoelectronic response was recorded using a source-measure unit (SMU), whose minimum integration time is on the order of tens of microseconds. To ensure a window that can reliably acquire complete attenuation and fit parameters, we used a conservative sampling configuration, which resulted in a coding window of about  $100 \mu\text{s}$ . This results in a total latency of  $0.8 \text{ ms}$  for one block. Further, in theory, the window can be compressed by faster readout and higher light intensity.

1151  
1152

### A.8 ACCURACY GAP ANALYSIS

1153  
1154  
1155  
1156  
1157  
1158  
1159  
1160  
1161

In this section, we show an analysis to separate the two sources of accuracy loss: the Quantization step (Full BERT to QNN) and the Otters implementation step (QNN to Otters). As the Table 7 shows, the main drop in accuracy occurs during the first step which is the expected performance loss from quantizing the model’s weights and activations. We then measured a second, much smaller accuracy drop when converting from the QNN to our Otters SNN. The average drop is 0.59%, which mainly comes from sampling errors (the exact physical time  $t_k$  needed for value  $O(t_k)$  might fall between two sampling points, causing a representation error). We believe this small accuracy trade-off is highly favorable, as the Otters implementation achieves this performance while consuming only 36.8% of the QNN energy.

1162  
1163  
1164

Table 7: Accuracy gap analysis on the GLUE benchmark, where all scores are accuracy except for STS-B (Pearson correlation).

1165  
1166  
1167  
1168  
1169

Model	QQP	MNLI-m	SST-2	QNLI	RTE	MRPC	STS-B	Avg
Full BERT	91.3	84.7	93.3	91.7	72.6	88.2	89.4	87.31
QNN	87.81	78.40	91.28	86.80	70.03	86.51	85.87	83.81
Otters	87.67	78.50	91.28	86.42	68.95	84.56	85.19	83.22

1170

### A.9 GENERALIZABILITY OF OTTERS

1171  
1172

Otters is proposed to optimize the temporal decay function and its subsequent multiplication by sampling the natural decay of an oxide optoelectronic synapse. In other words, Otters provides an analog alternative to digital matrix multiplication, which is a basic and commonly used unit in most models. Therefore, Otters has the potential to be applied to most network structures (or at least optimize parts of them) since it is an optimization for base units. In Table 8, we provide VGG/ResNet on CIFAR-10 with different time window size as an example to demonstrate the generalizability.

1179  
1180  
1181  
1182

Table 8: Top-1 accuracy (%) of SNNs converted from ResNet18 and VGG16 across different time steps  $T$ . The time steps  $T = 2^n - 1$  (for  $n = 2, 3, 4, 5$ ) are selected based on the n-bit QNN conversion discussed in Proposition 1.

1183  
1184  
1185  
1186  
1187

Model	Time steps $T$			
	3	7	15	31
Otters-ResNet18	89.27	89.31	92.02	92.05
Otters-VGG16	87.38	89.42	91.62	91.49

1188  
1189

## A.10 1-BIT KV ENERGY ABLATION STUDY

1190 In this section, we recalculate the energy of other SNN methods, assuming all K/V projections are  
 1191 quantized to 1-bit for a fair comparison with our Otters-1bitkv model. The spike rates and time  
 1192 window sizes are set to be consistent with those in Appendix A.3.1. As shown in Table 9, Otters still  
 1193 achieves the best energy efficiency within this 1-bit KV setting.

1194  
1195  
1196

Table 9: Energy consumption analysis on the SST-2 dataset. The Energy Ratio is Energy(Otters) / Energy(Model).

1197  
1198  
1199  
1200  
1201

Model	FC (mJ)	QKV (mJ)	Total (mJ)	Energy Ratio
Sorbet (1bit kv) (Tang et al., 2025)	3.39	0.58	11.32	2.79x
SpikingBERT (1bit kv) (Bal & Sengupta, 2024)	6.37	1.07	21.27	5.24x
SpikingLM (1bit kv) (Xing et al., 2024b)	2.09	0.35	6.97	1.72x
<b>Otters (1bit kv)</b>	<b>1.14</b>	<b>0.33</b>	<b>4.06</b>	<b>1x</b>

1202  
1203

## A.11 QNN-TO-SNN CONVERSION DISCUSSION

1204  
1205  
1206  
1207  
1208  
1209  
1210  
1211  
1212  
1213  
1214  
1215  
1216  
1217  
1218  
1219

Direct training of SNNs is challenging because the binary spike activation is non-differentiable. Instead of using approximate gradients, QNN-to-SNN conversion trains a functionally equivalent QNN first and transfers the weights to the SNN. This approach often yields higher accuracy for deep networks. Many related works have implemented this. For example, in language tasks, Sorbet achieves 79.80% accuracy on GLUE using an average spike generation method (Tang et al., 2025); for vision tasks, Wang et al. reach 85.31% on ImageNet using a Multi-basis Exponential Decay (MBE) neuron (Wang et al., 2025a). Liu et al. (Liu & Liu, 2018) propose quantization-aware DNNs using neuron convergence and weight clustering, and deploy the resulting 4-bit networks on memristor-based Spiking neuromorphic computing systems, achieving 90.33% for CIFAR-10. Beyond these, Ajay et al. (Ajay et al., 2024) introduce MC-QDSNN, a quantized deep evolutionary SNN that uses Multi-Compartment Leaky (MCLeaky) neurons for better and more efficient modeling of time-series data. However, most prior works rely on rate encoding and do not target optical hardware. In contrast, Otters focuses on TTFS-based SNNs using optical spiking neurons. To adapt QNNs to our  $\text{In}_2\text{O}_3$  devices, we propose specific conversion techniques, including dynamic thresholding and mapping quantization bits to the natural decay. This allows us to replace expensive digital matrix multiplication with energy-efficient analog sampling.

1220  
1221  
1222  
1223

## A.12 THE USE OF LARGE LANGUAGE MODELS

We use LLMs to aid or polish writing.

1224  
1225  
1226  
1227  
1228  
1229  
1230  
1231  
1232  
1233  
1234  
1235  
1236  
1237  
1238  
1239  
1240  
1241